Internal wave generation in a global baroclinic tide model

Harper L. Simmons[a,b,*], Robert W. Hallberg[b], Brian K. Arbic[c]

[a]*International Arctic Research Center, University of Alaska Fairbanks, Fairbanks, AL 99775, USA*
[b]*Geophysical Fluid Dynamics Laboratory, P.O. Box 308, Princeton, NJ 08542-0308, USA*
[c]*Program in Atmospheric and Oceanic Sciences, Princeton University, Princeton, NJ 08544-0710, USA*

Abstract

The energy flux out of barotropic tides and into internal waves (''conversion'') is computed using a global domain multi-layer numerical model. The solution is highly baroclinic and reveals a global field of internal waves radiating way from generation sites of rough topography. A small number of sites where intense internal wave generation occurs accounts for most of the globally integrated work done on the barotropic tide and dominates sites such as the Mid-Atlantic ridge. The globally integrated conversion of the M_2 barotropic tide is 891 Gigawatts and the globally integrated rate of working of the ocean by astronomical forcing is 2.94 Terawatts. Both of these estimates are close to accepted values derived from independent methods. Regional estimates of conversion are also similar to previous inferences, lending additional confidence that the solution has captured the essential physics of low-mode internal wave generation and that numerical prediction of conversion has skill in regions where no previous estimates are available.
© 2004 Elsevier Ltd. All rights reserved.

1. Introduction

Tidal forcing by the sun and moon acts as a body force on the ocean, and it responds by accelerating as a barotropic flow. Internal wave generation subsequently occurs as a result of the flow of the stratified ocean over topographic variations such as ridges, trenches, seamounts, and shelf breaks (e.g. Bell, 1975; Baines, 1982; Hibiya, 1986). This generation of internal waves

corresponds to a baroclinic wave drag and results in a transfer of energy out of the barotropic tide and into internal (baroclinic) waves. In this paper, we will refer to this flux as a ''conversion''. The area integrated conversion (Joules per second or Watts) is a rate of work, and has the same units as dissipation. The spatial redistribution of energy by propagating internal waves will be referred to as a baroclinic energy flux, and has units of Watts per meter. It should be understood that the energy extracted from the barotropic tide is not truly lost from the earth–sun–moon mechanical energy budget until it has been converted to heat by molecular viscosity. Some of the internal waves that are excited have high wavenumber and shear,

---

*Corresponding author. International Arctic Research Center, University of Alaska Fairbanks, Fairbanks, AL 99775, USA.

E-mail address: hsimmons@iarc.uaf.edu (H.L. Simmons).

generate turbulence, and hence are dissipated by viscosity quickly. Others have lower wavenumber and are relatively stable (St. Laurent and Garrett, 2002). These low wavenumber waves are rapidly organized into a modal structure and are free to radiate away from the generation site, provided they are not excited at their critical latitude where their group velocity is zero. There is also more immediate viscous dissipation in turbulent bottom boundary layers. Observational evidence for the radiation of tidal frequency low-mode internal waves over thousands of kilometers comes from satellite altimetry (Ray and Mitchum, 1996, 1997; Ray and Cartwright, 2001; Cummins et al., 2001), current meters (Hendry, 1977; Chiswell, 2002; Alford, 2003) and acoustics (Dushaw et al., 1995). The cascade of energy from the barotropic tide though internal tides to turbulence is the central topic of the HOME experiment (Rudnick et al., 2003).

We are interested in the internal tides because they are a contributor to the internal wave continuum (Munk, 1981). The dissipation of tidal energy is also of inherent interest because of the implications for classical geophysical problems such as the length of the day and the evolution of the earth–moon system. Astronomical inference constrains the total dissipation of tidal energy in the earth–sun–moon system to be 3.7 Terawatts (TW), with 3.5 TW dissipated in the ocean (Munk, 1997; Egbert and Ray, 2001). Analysis of the tides using analytical methods, altimetry, and tidal modeling suggests that approximately 2.5 TW of this energy loss occurs through turbulent dissipation by direct dissipation in bottom boundary layers, primarily in shallow waters, and does not contribute to interior diapycnal mixing.

Observed turbulent diffusivities in the ocean interior range from $0.1\,cm^2\,s^{-1}$ in the thermocline (Ledwell et al., 1993, 1998) to greater than $10\,cm^2\,s^{-1}$ in the deep ocean above rough topography (Polzin et al., 1997; Ledwell et al., 2000). The main source of this energy is the internal wave field of the ocean. Munk and Wunsch (1998) calculated that 2 TW must be dissipated throughout the ocean to sustain a bulk turbulent diffusivity of $1cm^2\,s^{-1}$, maintaining the observed density stratification against an assumed over-

turning rate [although this amount has been disputed by Webb and Suginohara (2001)]. One Terawatt of energy loss from the barotropic tide has been attributed to internal tide generation, the subject of this paper. Previously, the global distribution of energy flux into the internal tides has been examined using theory (Sjöberg and Stigebrandt, 1992; Morozov, 1995), and tidal models (Kantha and Tierney, 1997; Egbert and Ray, 2000, 2001; Jayne and St. Laurent, 2001). Observational studies have shown that mixing rates are enhanced in regions of internal tide generation (Kunze and Toole, 1997; Lueck and Mudge, 1997; Polzin et al., 1997; Ledwell et al., 2000; Lien and Gregg, 2001; Pinkel et al., 2001; Kunze et al., 2002; Moum et al., 2002).

Previous estimates of the spatial distribution of energy sinks for the barotropic tides have used data-assimilative hydrodynamic models or theory. Morozov (1995) estimated 1.1 TW for the M_2 tide. Egbert and Ray (2001) estimated 0.70 ± 0.15 TW for the M_2 tide and 1 ± 0.25 for all lunar and solar constituents, but suggested that their estimate is conservative. Egbert and Ray (2001) have described the loss of energy from the barotropic tides as a energy sink term in the shallow water equations (see Section 2.3). Misfit between the hydrodynamic model and the assimilated altimeter data was attributed to "dissipation" of the barotropic tide by unresolved internal wave generation. This results in an estimate of total dissipation of the barotropic tide, but does not differentiate between the unresolved generation of low-mode internal waves of tidal frequency ("internal tides") and direct frictional dissipation. Furthermore, while Egbert and Ray's estimate of energy input is compelling and is strongly constrained by the altimeter data, it is not a *direct* calculation of the energy input into internal tides because those dynamics are precluded from their barotropic model, and their estimate hinges on the premise that their model misfit was primarily due to the missing physics of internal tide generation, and not due to intrinsic model error.

Baines (1973, 1982) estimated the conversion rate analytically. He considered a rotating, stratified, linearized, inviscid fluid, and decomposed the flow into a baroclinic component and a barotropic

component with equivalent sea surface height expression. This reduces the problem to the determination of the solution for the barotropic flow and the computation of the additional flow required to satisfy the original stratified dynamics and boundary conditions. The form of this additional term was interpreted as a ''body force'' on the barotropic tide. Baines calculated the adiabatic body forcing of the internal tides for simple solutions for the tidal flow in idealized two-dimensional geometries.

There have been a large number of regional numerical simulations of baroclinic tides. Studies include Kang et al. (2000), who studied baroclinic energy fluxes away from Hawaii using a regional two layer tide model, Kowalik and Polyakov (1999), who studied diurnal tides over Kashevarov Bank, as well as studies by Cummins and Oey (1997), Xing and Davies (1998), Holloway and Merrifield (1999), Cummins et al. (2001), and Merrifield et al. (2001). Niwa and Hibiya (2001) diagnosed barotropic to baroclinic conversion in the Pacific Ocean in an ocean model using the analytical Baines body force. Quantitative comparisons with results from many of these studies will be discussed in Section 4.

Although there have been a number of previous attempts to quantify the global input of energy into the internal wave field of the ocean, there have been no previous direct calculations of either the global internal wave field or the conversion rate that could unambiguously implicate internal wave generation by the tides as being responsible for the missing TW of energy loss from the barotropic tide. Our goal is to investigate the phenomena of barotropic-to-baroclinic mode conversion, internal wave generation, and energy redistribution by baroclinic energy flux in a process-oriented manner, using a high resolution baroclinic tide model. To this end, we will consider an initially quiescent, stratified ocean. Significantly, the ocean will be adiabatic. The motivation for this is that we wish to avoid any parameter dependence on sub-grid-scale parameterization of turbulence, we wish to consider the internal wave generation in the adiabatic limit, and we hypothesize that adiabatic low-mode internal wave generation can account for the TW of energy loss from the barotropic tide.

While the model does have viscous stresses, it is adiabatic in the sense that there is no diapycnal mixing and hence the water mass census remains fixed for all time. In a companion study (Arbic et al., 2004), we also explore baroclinic tides in a global model. The distinction between that study and the present one is that in Arbic et al. (2004) the accuracy of the surface tides is the goal, and baroclinicity is shown to improve the fidelity of simulations of the surface tide, whereas here our motivation is to focus on the internal wave generation itself.

2. The vertically integrated primitive equations

Because the barotropic tides and their scattering of energy to internal waves is naturally represented by a modal description, an isopycnic coordinate ocean model is a natural tool for investigating the energetics of internal tides. We use the Hallberg Isopycnal Model (Hallberg and Rhines, 1996). Fig. 1 illustrates the relationship between the isopycnal coordinate system used by the model and the geopotential coordinate system. In isopycnal coordinates $z_{1/2} = \eta$ is the free surface displacement, and the subsequent interface elevations are measured from the resting sea surface height ($z = 0$). Interface thickness, h_n is the positive definite distance between adjacent interfaces, i.e., $h_n = z_{n-1/2} - z_{n+1/2}$. The ocean floor $-H(x, y)$ is rigid, though for our subsequent development of an energy equation this is not necessary. Tidal forces and loading do in fact
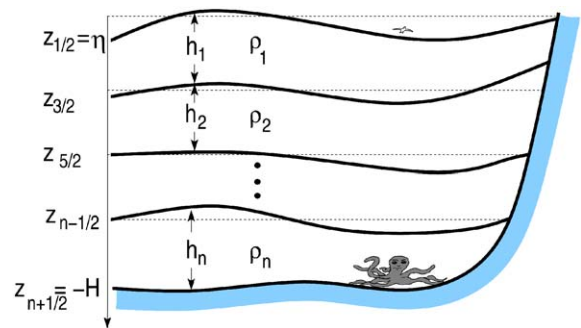

Fig. 1. Schematic for shallow water equations.

cause the ocean floor to deflect, and this should be accounted for in our energy equations because of the associated modification of the reference level for calculation of potential energy. Here, we account for the deformation of the ocean bottom in the traditional manner, via the Love numbers and a scalar approximation to self-attraction and loading (Section 2.1), and take the ocean bottom as fixed in time. This is appropriate at this stage for our process-oriented approach to the energetics of the tides.

The Boussinesq, adiabatic, hydrostatic, and nonlinear shallow water momentum equations are written for each layer as

$$\frac{\partial}{\partial t}\boldsymbol{u}_n + (\zeta_n + f)\hat{\boldsymbol{k}} \times \boldsymbol{u}_n$$
$$= -\nabla\left(M_n + \frac{1}{2}\boldsymbol{u}_n^2 + g\Pi\right) + \boldsymbol{H}_n + \boldsymbol{V}_n. \qquad (1)$$

$\zeta_n = \hat{\boldsymbol{k}} \cdot (\nabla \times \boldsymbol{u}_n)$ is the relative vorticity. M_n is the nth layer perturbation Montgomery potential, which is the layer integrated analogue to perturbation geopotential pressure. It is defined recursively as

$$M_1 = g_{1/2}\eta, \quad M_{n+1} = M_n + g_{n+1/2}\, z'_{n+1/2},$$

where $g_{n+1/2} = g(\rho_{n+1} - \rho_n)/\rho_n$, and $z'_{n+1/2}$ is the departure of the interface from its resting depth. For the first interface ($n = \frac{1}{2}$), $g = g_{1/2}$ is the full gravity. Tidal forcing, $g\Pi$, is in the form of the gradient of a potential. Details of this forcing are described in detail in Section 2.1. Momentum is diffused vertically by $\boldsymbol{V}_n$, a quadratic drag at the

ocean bottom, and horizontally by $\boldsymbol{H}_n$, a biharmonic diffusion operator.

The continuity equation for each layer takes the from of a thickness tendency equation and is written as

$$\frac{\partial}{\partial t}h_n + \nabla \cdot (\boldsymbol{u}_n h_n) = 0. \qquad (2)$$

Details of the finite difference numerical solution to (1) and (2) can be found in Hallberg and Rhines (1996) and Hallberg (1997). We will use the split time stepping scheme of Hallberg (1997). This scheme splits (1) into a computationally inexpensive but rapidly evolving barotropic mode, and a slowly evolving but computationally expensive baroclinic mode. These modes are defined in Section 2.3.

2.1. Tidal forcing

Tidal forcing (Π) arising from the eight primary constituents (M2, S2, N2, K2, K1, O1, P1, Q1) (Gill, 1982 and Table 1) has been added to the momentum equations. The formulation follows Marchuk and Kagan (1984), by considering a tide generating potential $g\Pi_{eq}$ with corrections due to both the earth tide $(1 + k - l)$ and a scalar approximation to self-attraction and loading ($\alpha\eta$). Thus the full tidal potential in (1) is

$$g\Pi = g(1 + k - l)\Pi_{eq} + g\alpha\eta. \qquad (3)$$

The *equilibrium tide*, Π_{eq}, arises from the astronomically derived gravity producing forces. It is modified by several factors. The Love numbers, k and l account for the reduction of the ocean tide

Table 1
Frequencies (ω), Love numbers (k and h), and amplitude (a) functions for the eight principle constituents of tidal forcing

Constituent	Name	Origin	ω ($\times 10^{-4}\,\mathrm{s}^{-1}$)	$1 + k - l$	a (m)
1	K_1	Luni-solar declinational	0.7292117	0.736	0.141565
2	O_1	Principal lunar declinational	0.6759774	0.695	0.100661
3	P_1	Principal solar declinational	0.7252295	0.706	0.046848
4	Q_1	Larger lunar elliptic	0.6495854	0.695	0.019273
5	M_2	Principal lunar	1.405189	0.693	0.242334
6	S_2	Principal solar	1.454441	0.693	0.112743
7	N_2	Larger lunar elliptic	1.378797	0.693	0.046397
8	K_2	Luni-solar declinational	1.458423	0.693	0.030684

because of the yielding of the solid earth by tidal forces (l) and from the perturbation of the potential due to the redistribution of mass within the earth caused by the yielding (k). The Love numbers are frequency dependent, with $1 + k - l$ generally close to 0.7 (Wahr, 1981). The term α in (3) provides a scalar approximation to the modification of the ocean's tidal response as a result of self-attraction and loading (SAL) (Hendershott, 1972). Rigorous determination of SAL requires an extremely cumbersome integration over the earth surface, rendering a proper treatment of the tidal equations an integro-differential equation (Ray, 1998). Limitations of the scalar approximation to SAL are discussed by Ray (1998), who concluded that the scalar approximation introduces phase errors of up to $30°$ and amplitude errors of 10% into a global scale tidal simulation.

The equilibrium tide is written for the jth diurnal tidal constituent as

$$\Pi_{\text{eq},j} = a_j \sin 2\phi \cos(\omega_j t + \lambda) \tag{4}$$

and for the jth semidiurnal constituent as

$$\Pi_{\text{eq},j} = a_n \cos^2 \phi \cos(\omega_j t + 2\lambda), \tag{5}$$

where ϕ is latitude and λ is longitude. The frequencies (ω_j), amplitudes (a_j) and Love numbers are listed in Table 1. Recognizing that Eqs. (4) and (5) require the computationally expensive evaluation of trigonometric functions at every grid point and every time-step, tidal forcing is introduced in the following mathematically equivalent form. Making use of the identity $\cos(A + B) = \cos(A)\cos(B) - \sin(A)\sin(B)$, we can write the eight tidal forcing constituents as

$$
\begin{aligned}
\Pi_{\text{eq}} = \sum_{j=1}^{4} [&\beta_j \quad a_j \quad \cos^2 \phi [\cos(\omega_j \quad t)\cos 2\lambda \\
&- \sin(\omega_j \quad t)\sin 2\lambda] \\
&+ \beta_{j+4} a_{j+4} \sin 2\phi [\cos(\omega_{j+4} t)\cos 2\lambda \\
&- \sin(\omega_{j+4} t)\sin 2\lambda]],
\end{aligned} \tag{6}
$$

which allows all the trigonometric functions of ϕ and λ to be pre-computed. Note that we have written $\beta_j = 1 + k_j - l_j$. When mode-splitting is employed, tidal forcing is added only to the

barotropic equations. In Section 2.3, we will show analytically that tidal forcing should not appear in the baroclinic mode.

2.2. Energetics of the vertically integrated primitive equations

We wish to construct an energy budget in order to determine the work done by the tides and friction. For simplicity we will use the horizontally continuous equations here, but the constructed budget will actually be calculated from the horizontally discrete terms in the model. Our budget is constructed through the operation $h_n \boldsymbol{u}_n \cdot (1) + \frac{1}{2} \boldsymbol{u}_n^2 \cdot (2)$, and gives

$$
\begin{aligned}
\boldsymbol{u}_n h_n &\frac{\partial \boldsymbol{u}_n}{\partial t} + \frac{1}{2} \boldsymbol{u}_n^2 \frac{\partial h_n}{\partial t} \\
&= -\boldsymbol{u}_n h_n \nabla M_n - g\boldsymbol{u}_n h_n \nabla \Pi + \boldsymbol{u}_n h_n \\
&\quad \times \left[(\zeta_n + f)\hat{\boldsymbol{k}} \times \boldsymbol{u}_n - \nabla \left(\frac{1}{2} \boldsymbol{u}_n^2 \right) \right] - \frac{1}{2} \boldsymbol{u}_n^2 \nabla \cdot (\boldsymbol{u}_n h_n) \\
&\quad + \boldsymbol{u}_n h_n \boldsymbol{H}_n + \boldsymbol{u} h_n V_n.
\end{aligned} \tag{7}
$$

Note that for our Boussinesq model, a constant factor of ρ_0 (the mean density of the ocean) will need to be multiplied through our energy density equation in order to obtain the traditional units for energy. Because the model conserves both mass and momentum, a budget constructed in this manner will close by construction. The two terms on the left-hand side are the time tendency of kinetic energy density. The first term on the right-hand side is the kinetic-to-potential energy conversion. The next term is the work done on the ocean by the tidal forces. The next three terms are the Coriolis and advection terms. The final two terms are the energy sinks due to the horizontal and vertical viscous stresses.

We can construct an available potential energy budget through the operation $M_n \cdot (2)$, giving us

$$M_n \frac{\partial}{\partial t} h_n + M_n \nabla \cdot (\boldsymbol{u}_n h_n) = 0. \tag{8}$$

Adding (7) and (8) gives a total energy equation.

At this point a number of manipulations of an energy budget based on vector and product rule identities appropriate to the continuous equations could be made such as recasting it into

flux-divergence form, but since our guiding principle is to construct an energy budget which applies strictly to our model momentum and continuity equations, these traditional manipulations are foregone. Note also that the Coriolis term is retained. While it drops out of the continuous equations point-wise because of a simple vector identity, this is not true of the discrete equations. The Coriolis terms here use the Sadourny (1975) energy conserving discretization, which would identically vanish upon global integration if a non-split time-stepping scheme were used. With a split time stepping scheme, the global cancellation is not perfect, but this term is six orders of magnitude smaller than the leading terms. The discrete energy budget has been constructed following the derivation of the energy budget from the continuous equations and it balances by construction. However, unless a trapezoidal time stepping scheme is used, the time-discretized first two terms in (7) are not guaranteed to exactly agree with the time derivative of thickness weighted kinetic energy density, i.e.,

$$\boldsymbol{u}h \frac{\partial \boldsymbol{u}}{\partial t} + \frac{1}{2} \boldsymbol{u}^2 \frac{\partial h}{\partial t} \neq \frac{1}{2} \frac{\partial h \boldsymbol{u}^2}{\partial t}.$$

In a non-split case, these differences are small and result purely from temporal truncation errors. In the split-explicit case, there is an additional complicating factor. With a split time stepping scheme, there are two estimates of the free surface height—one from the sum of the layer thicknesses, the other from stepping forward the external mode equation. A positive definite continuity solver must be used for the layer thicknesses, but as there is no positive definite continuity solver that is linear in the layer thicknesses, the two estimates do not agree. The difference between these two estimates must be reconciled somehow—either by dilating all of the layers (Bleck and Smith, 1990), iterating the barotropic solution (Paul Schopf, pers. comm.), or by adding a fictitious mass source to the barotropic solution that sets up a divergent barotropic flow field an drives the two solutions toward each other, as is done here. This latter solution is efficient and has worked quite well for simulations of low-frequency flows. Unfortu-

nately, the difference radiates as short-wavelength external gravity waves, and this shows up in the energetic analysis as a spurious energy source in the time tendency of kinetic energy. In hindsight, it would have probably been preferable to use the diabatic solution of dilating the layers to match the external calculation (Bleck and Smith, 1990). Fortunately this energy source is still only a few percent of the tidal forcing, and these waves tend to be of such short wavelengths that they are effectively dissipated by the horizontal viscosity. Further, as they have frequencies that are higher than those of the shortest resolved internal waves (and in our many-layer case higher than the buoyancy frequency), there is no linear conversion to baroclinic waves—the primary focus of this study. Based upon comparisons between split and un-split simulations we find that this fictitious energy source does not have a qualitative impact on the tidal solutions and analysis presented here, provided the degree of splitting is eight-to-one or less.

2.3. Modal energy equations

In the previous section, we transformed the model's momentum equations into a total kinetic energy budget in order to quantify the balance between energy input by tidal forces and dissipation by friction. In order to quantify the energy input into the baroclinic internal waves by inviscid, adiabatic processes, we now derive *modal* energy equations for an inviscid version of our layered system. For simplicity, we will work with the linearized momentum equations. It is straightforward to include the nonlinear terms (ζ_n and $\boldsymbol{u}^2$), but is more algebraically complicated. We neglect them a posteriori in our derivation as these terms are $O(u^3)$ in our energy equation. Furthermore, these terms were diagnosed to be two orders of magnitude smaller than the linear terms over most of the domain. We define the barotropic mode velocity and Montgomery potential as their thickness weighted average. For velocity, this is

$$\bar{\boldsymbol{u}} = \frac{1}{\Sigma_{n=1}^{k} h_n} \sum_{n=1}^{k} h_n \boldsymbol{u}_n, \tag{9}$$

where k is the total number of layers. The baroclinic mode is the departure from the thickness weighted average ($u'_n = u_n - \overline{u}$). By this definition the thickness weighted vertical averaged of a baroclinic quantity vanishes.

Substituting $u_n = \overline{u} + u'_n$ and $M_n = \overline{M} + M'_n$ into (1) and (2), neglecting $O(u^3)$ and viscous terms, we obtain a budget for the barotropic mechanical energy density for each layer through the operation $h_n\overline{u} \cdot (1) + \overline{M} \cdot (2)$. Summing over all layers and eliminating any terms that will vanish upon vertical summation, this yields

$$\sum_{n=1}^{k}\left[\overline{u}h_n\frac{\partial\overline{u}}{\partial t} + \overline{M}\frac{\partial h_n}{\partial t}\right]$$
$$= \sum_{n=1}^{k}[-g\overline{u}h_n\nabla\Pi - \nabla\cdot(\overline{u}h_n\overline{M}) - \overline{u}h_n\nabla M'_n]. \quad (10)$$

Similarly, a baroclinic mechanical energy budget is obtained through the operation $h_n u'_n \cdot (1) + M'_n \cdot (2)$, yielding

$$\sum_{n=1}^{k}\left[u'_n h_n\frac{\partial u'_n}{\partial t} + M'_n\frac{\partial h_n}{\partial t}\right]$$
$$= \sum_{n=1}^{k}[-\nabla\cdot(u'_n h_n M'_n) + \overline{u}h_n\nabla M'_n]. \quad (11)$$

The term

$$J = \sum_{n=1}^{k} u'_n h_n M'_n \quad (12)$$

is the depth-integrated baroclinic energy flux vector. The term

$$C = \sum_{n=1}^{k} \overline{u}h_n\nabla M'_n \quad (13)$$

is leading order depth-integrated barotropic-to-baroclinic energy conversion, and is balanced by the same term, but of opposite sign in the barotropic energy density equation (10). Note that the tidal forcing, $u'_n h_n\nabla\Pi$, is eliminated from our depth-integrated baroclinic energy budget (11) by our definition of baroclinicity—the tidal forces do not input energy into the baroclinic mode.

3. Description of numerical experiments

The vertical coordinate is potential density referenced to 2000 m (σ_2). We explored using a realistic stratification as an initial condition, but found that even after a month the ocean was still experiencing large-scale adjustment that precluded a simple extraction of the tidal signal. Although we will continue to explore this approach, it proved to introduce too many challenges at this stage. For this reason, we elected to set the initial condition to a state of rest, with a single, horizontally uniform stratification profile (zero available potential energy), based on a zonal mean of the Subtropical North Pacific (Fig. 2) computed from the 1998 World Ocean Atlas (Antonov et al., 1998; Boyer et al., 1998). This stratification is representative of most of the world ocean, but clearly cannot represent high latitudes well.

From this profile, we configured two and 10 layer experiments. The two layer experiments were constructed by averaging σ_2 from our profile into two bins, one for waters from the surface to 1100 m in depth, and the other for waters from 1100 m to the ocean bottom, so that active interfaces lie at the surface and 1100 m depth.
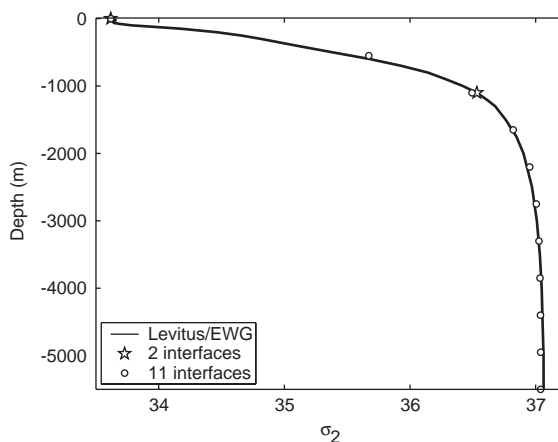

Fig. 2. Zonal mean potential density referenced to 2000 m (σ_2) for the Pacific, with two (star) and 10 (circles) layer densities and interface depths indicated. The two-layer solution has two active interfaces, one at the free surface, the other at 1100 m. The 10-layer solution has 11 active interfaces that are separated by 550 m layers.

For 10 layer experiments, the profile was constructed by equipartitioning σ_2 into 550 m thick layers. In this latter case, the third interface lies at the same depth, 1100 m, as the second interface in the two-layer experiments. By choosing equal thickness layers, we ensure that topography at all depths can interact with "local" stratification even though this would not be the optimal distribution for representing the flat-bottom normal modes, as might be suggested by Wentzel–Kramer–Brillouin (WKB) stretching. The rationale for considering two layers is that this system, by construction, cannot support higher modes and there is an interest in the relatively simple and energetically dominant gravest internal mode response. A two layer system is also computationally inexpensive. The 10 layer system is still computationally feasible for a single constituent and can be used to examine higher-mode conversions.

The horizontal grid covers the globe with a uniform spherical grid at one-eighth degree resolution from 78°S to 65°N. Above this latitude, the grid transitions to a bipolar grid (Murray, 1996) that allows polar regions to be resolved without a coordinate singularity occurring over the ocean. A characteristic of this grid is that the ocean resolution north of 65°N is nearly a uniform rectangular grid with a horizontal grid resolution close to the longitudinal resolution of the spherical grid at 65°N. Additional details of the model configuration can be found in Appendix A.1. Our simulations are all started from a state of rest. Runs presented in the main body of the text are forced with only a single semidiurnal constituent, M_2. A solution forced with a single frequency obviates the need to average over long period "beats" that occur (such as fortnightly tides as well as longer periods) when multiple constituents are included. The M_2-only configuration is of particular interest, as it is the dominant constituent by approximately a factor of two in amplitude (Table 1), and there is an extensive literature devoted to this constituent. Because the tides in the deep ocean are nearly linear, it is fortunately possible to learn much from running with a single constituent. Nonetheless, we acknowledge that interactions between components is an important physical process. Some discussion of

experiments with eight constituents will occur in Appendix A.2, but more extensive discussion will be deferred to a future publication. While many more experiments were conducted in order to assess the sensitivity of C and J to various model parameters, forcing and resolution, our two and ten layer experiments capture much of the essential physics. Details of the additional configurations and their results can be found in Appendix A.2.

4. Results

A practical idealization necessary for this study was the use of a horizontally uniform stratification. While this eliminates transient wave adjustment, and allows us to examine the baroclinic wave generation in an otherwise resting ocean, it distorts the physics of conversion and internal wave energy flux. We can think of our horizontally uniform ocean as having been subjected to a WKB-like normalization such that the thermocline depth and non-rotating gravity wave speed are horizontally constant. WKB normalization is commonly used in the presentation of observational data as a convenience to facilitate comparison between regions of differing stratifications (Leaman and Sanford, 1975; Althaus et al., 2003). In order to approximately "correct" our estimates to account for the observed variation of topography, we will apply an a posteriori "renormalization" of energy flux and conversion by

$$(\hat{C}, \hat{J}) = (C, J)\left(\frac{\Delta\rho(x,y)}{\Delta\rho_0}\right)^{1/2} \qquad (14)$$

and isopycnal displacement by

$$\hat{\eta} = \eta\left(\frac{\Delta\rho_0}{\Delta\rho(x,y)}\right)^{1/4}. \qquad (15)$$

$\Delta\rho_0$ is the potential density difference between the upper and lower layer in our two-layer model and $\Delta\rho(x,y)$ is the climatological map of spatial varying potential density difference between waters above 1100 m and those below. The caret denotes renormalized quantities that might have been realized had the model been run with a
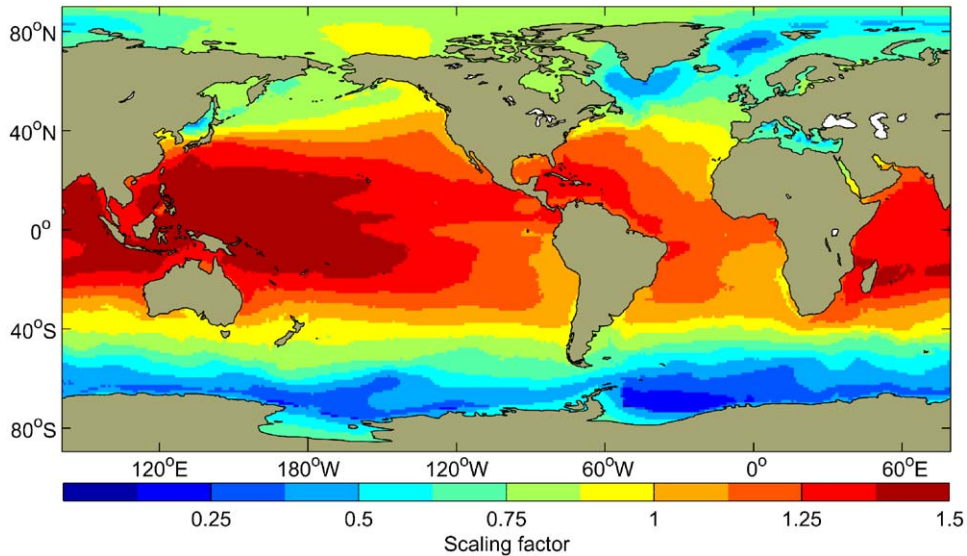
Fig. 3. Map of the multiplicative scaling factor used in (14) used to adjust our diagnosed energy flux and conversion rate for the neglected geographic variation in stratification. Note that this scaling factor is actually fairly modest, with the zonal mean value ranging from 0.4 to 1.3. To adjust internal isopycnal displacement we use the inverse square-root of this field (i.e., Eq. (15)).

non-uniform stratification. Subsequently reported conversion rates and fluxes will be rescaled using (14), and isopycnal displacements will be rescaled using (15). A map of the energy scaling factor (Eq. (14)) is shown in Fig. 3. Note that the magnitude of the renormalization is actually fairly modest with the zonal mean value of the scaling factor in (14) ranging from 0.4 to 1.3.

4.1. Generation of internal waves

The integration begins from a state of rest. We find that the tides energetically equilibrate within about 15 days, or about 30 M_2 periods (Fig. 4). The model is integrated for 21 days, with our analysis based on an average over the last two tidal cycles. Horizontal friction is relatively weak and once the model has equilibrated, the average tidal work over several tidal cycles is approximately balanced by the vertical friction in the system (Table 2). In the absence of numerical mode-splitting (Section 2.3) the balance between energy input by tidal forcing (T) and dissipation (ΣF) was found to be nearly exact. With a split time stepping scheme, the imbalance is still less

then 10%. The small mismatch between forcing and dissipation is balanced by the small but spurious time tendency of kinetic energy term (the first term in Eq. (7)) alluded to in Section 2.3. When all terms in (7) are included, the residual imbalance is six orders of magnitude less than the leading order steady-state balance between forcing and dissipation.

The main features of the barotropic tides are set up within a few tidal periods, with basin scale Kelvin waves propagating around the ocean basins (Fig. 5). As the ocean sloshes back and forth across rough topography, internal waves are generated (Figs. 6–8), which propagate away from numerous hot-spots. These waves are clearly seen as an isopycnal displacement, with amplitudes of order 20 m, but in some selected regions the displacements are an order of magnitude larger. After 20 days, a complicated "sea" of internal waves has saturated the ocean basins. One of the key features of the fully developed internal wave field are the large wavelengths approaching the critical latitudes ($\omega = f$ at 74.5° for the M_2 tide). This will be discussed further in Section 4.3. Note the complicated basin scale interference patterns,
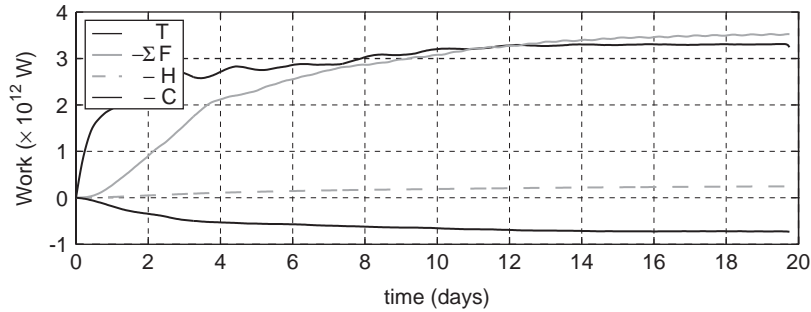
Fig. 4. Time-series of various terms in global energy budget. The data has been low-pass filtered to remove the (considerable) semidiurnal variability. The labels in the legend are T, the total work by the tidal forcing, ΣF, the total work done by friction, $-H$, the work done by horizontal friction, and C, the barotropic to baroclinic conversion rate. Dissipation is multiplied by negative one here for the purpose of visualization, so that if the traces of T and $-\Sigma F$ were exactly coincident, they would be in perfect balance.

Table 2
Globally integrated renormalized convergence rate ($\hat{C}$), work by vertical (V) and horizontal (H) friction, and work done by tides (T)

EXP	$\hat{C}$ (GW)	V (TW)	H (TW)	T (TW)
Two layer	671	3.18	0.20	3.17
Ten layer	891	2.71	0.45	2.94

Units for $\hat{C}$ are Gigawatts, units for V, H, and T are Terawatts.

and the tidal beams that appear to maintain their signatures over thousands of kilometers.

4.2. Barotropic tides

The barotropic tides are the forcing for our internal tides and therefore it is appropriate to assess their fidelity. A simple measure of the quality of the barotropic tidal solution can be made via a comparison between the computed surface tides and results from a very accurate data-assimilative model, TPX0.6 (Egbert and Erofeeva, 2002). TPX0.6 has absolute root-mean-square (RMS) discrepancies for the M_2 tide of less than 3 cm in water deeper than 1000 m. Fig. 5 shows M_2 tidal maps from the two-layer solution and from TPX0.6. Although certain features of the tidal solution are different, the overall amplitude and phase is qualitatively similar. For example, the major amphidromic systems of the Pacific, Indian, and Atlantic oceans are in the right locations, and

the spatial pattern of tidal amplitudes are reproduced well. The main region of discrepancy is the Southern Ocean. The wiggles in the phase that are particularly evident in our solution in the North Pacific are the surface manifestation of internal waves. They are also seen in altimeter data (see, e.g., Dushaw, 2002 and references therein), but are not in TPX0.6, which assimilates a low-pass filtered version of the altimeter data, and uses a barotropic model for hydrodynamic interpolation.

Our two-layer barotropic solution are more energetic than observed, with correlations of $R^2 = 0.91$ for amplitude and $R^2 = 0.60$ for phase. Our solution is of comparable accuracy to that of forward models of tides without a gravity wave drag scheme, but is less accurate than forward models with a gravity wave drag parameterization that has been carefully tuned (Jayne and St. Laurent, 2001; Arbic et al., 2004; Egbert et al., 2004). We believe that for the goals of this study (i.e. a process-oriented investigation of internal tide generation) the quality of our solutions are sufficient.

4.3. Baroclinic response

The strong baroclinicity of the tidal response is clearly evident in a section of meridional velocity shown in Fig. 9. The velocity in the upper ocean is in many places 180° out of phase with the barotropic current, and it is surface intensified. Near the ocean bottom, in the vicinity of
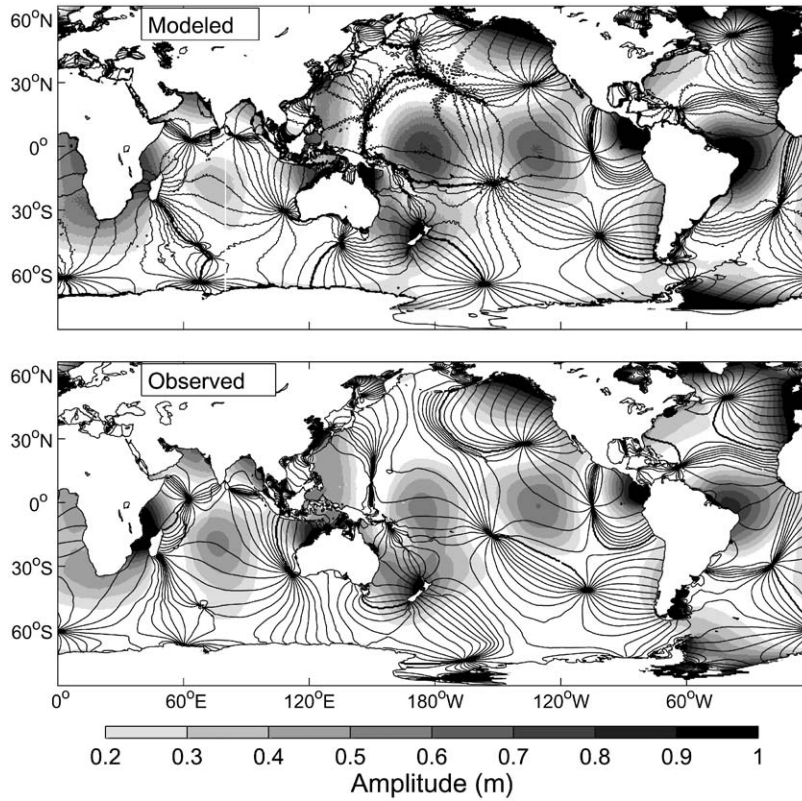
Fig. 5. M_2 tides from our M_2 only solution ("Modeled"), and from TPX0.6 ("Observed"), a very accurate data-assimilative tide model.
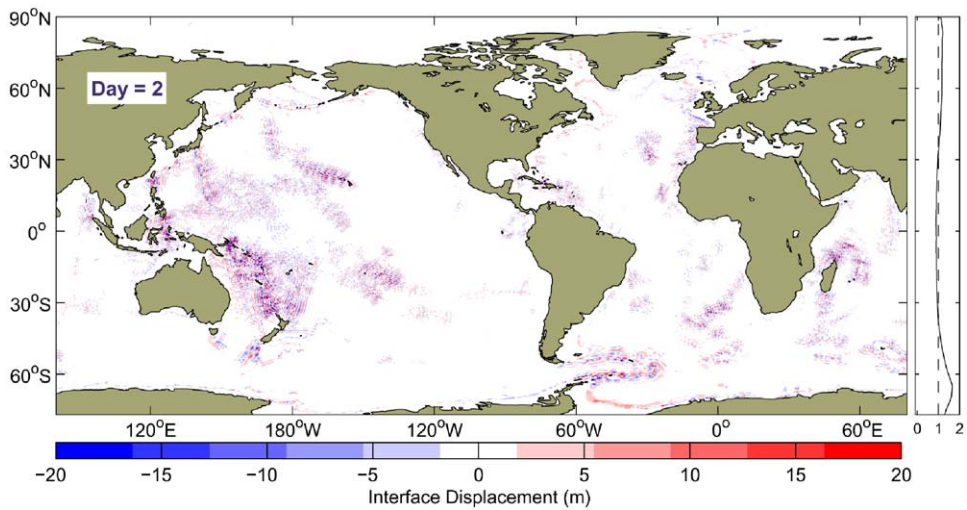

Fig. 6. Interface displacement, $\hat{\eta}$, normalized according to Eq. (15), on day two of spinup of the two-layer M_2 simulation. The resting depth of the interface is at 1100 m. The zonal mean of the normalization factor is shown on the right side of the plot.
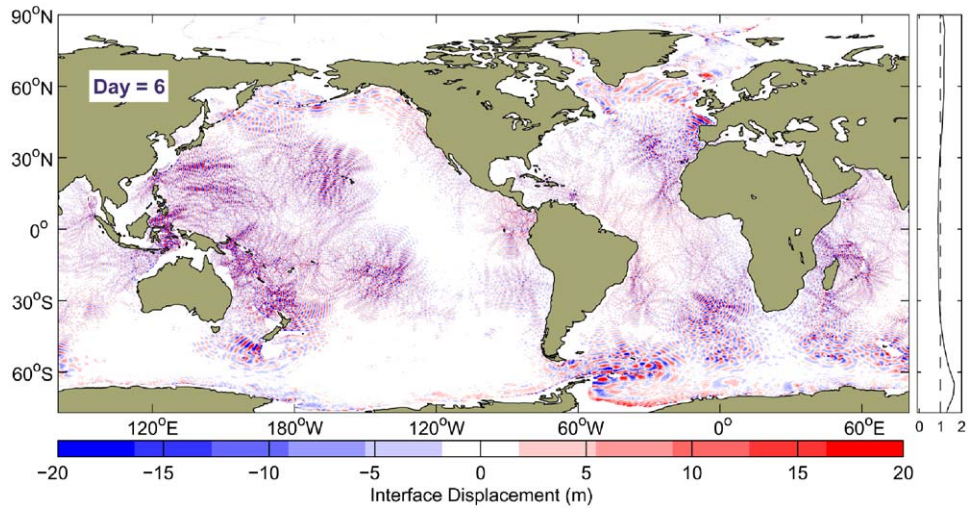
Fig. 7. Interface displacement, $\hat{\eta}$, normalized according to Eq. (15), on day six of spinup of the two-layer M_2 simulation. The resting depth of the interface is at 1100 m. The zonal mean of the normalization factor is shown on the right side of the plot.
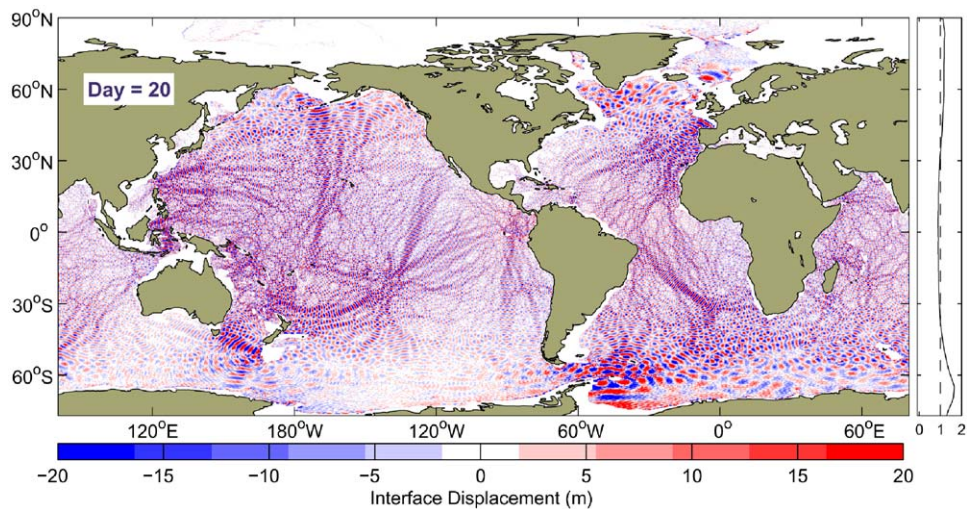

Fig. 8. Interface displacement, $\hat{\eta}$, normalized according to Eq. (15), on day 20 of spinup of the two-layer M_2 simulation. The resting depth of the interface is at 1100 m. The zonal mean of the normalization factor is shown on the right side of the plot.

roughness elements, small-scale disturbances to isopycnals are evidence for a low energy, higher mode response. A plan view from our two-layer experiment, comparing the depth-integrated flow with the upper layer flow is shown in Fig. 10. The striking difference between the upper layer flow (right panel) and the barotropic flow (left panel) is another indication of the baroclinicity of the tidal response. Note that while the barotropic flow is evident in the surface flow, it is mostly obscured by the many regions where the flow direction alternates direction at the wavelength of the internal tides, with larger magnitude than the large-scale barotropic flow. In these regions a comparison between a shallow water equations tidal solution and in situ current meter data could be as much as
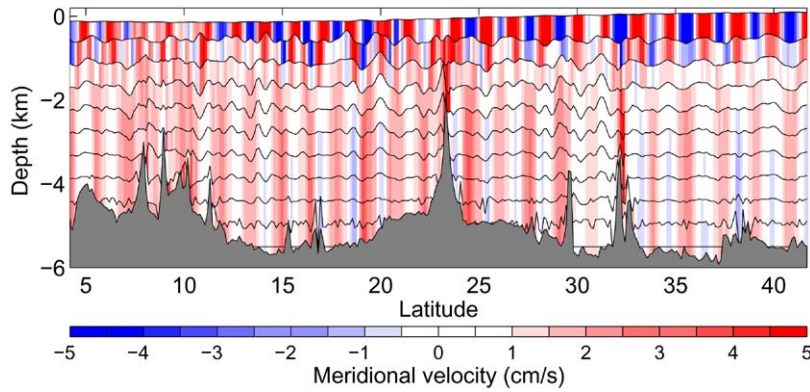
Fig. 9. Meridional section of meridional velocity in the Hawaiian Islands through Kauai Channel (approximately 159°W) for our 10 layer solution. Velocity is shaded between bounding isopycnals. Relative to the vertical scale of the plot, the ocean surface has been given a vertical scale exaggeration of 500, and interior isopycnals are exaggerated by a factor of 10.
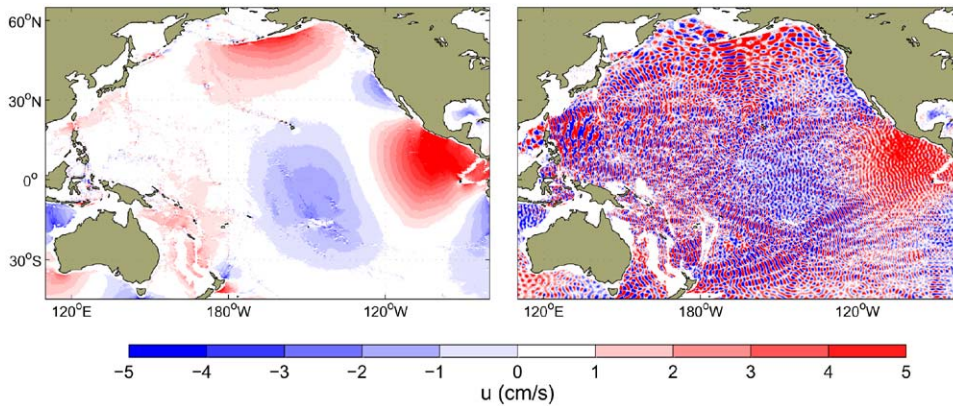

Fig. 10. Zonal component of velocity at day 20 of the two-layer M_2 simulation. Left panel: depth-integrated flow. Right panel: upper layer flow. For the purpose of visualization velocity has been set to zero for regions where water depth is less than 2200 m, so that we are only viewing flow where the lower layer is at least as thick as the upper layer (1100 m).

180°out of phase, and hence agreement would be very poor. Kowalik and Polyakov (1999) made such a comparison in the Sea of Okhotsk, and found reasonable agreement for current *amplitudes*, but found that direction was completely out of *phase* when compared with a shallow-water equations tide solutions. Agreement with observations was excellent when baroclinicity was included.

Another interesting feature of the solution is the small spatial scales evident in the interfacial waves near the equator (see, e.g., Fig. 8), and the larger wavelengths at higher latitudes. Note for example the large spatial scales in the vicinity of Drake Passage and in and around the Labrador Sea. The dispersion relationship for internal-mode gravity waves in the rotating, linear, hydrostatic two-layer system is given by

$$||k|| = \sqrt{\frac{(\omega^2 - f^2)H}{g'h_1h_2}}, \tag{16}$$

where k is the wavenumber, H is the total ocean depth, g' is the reduced gravity of the two-layer system, and ω is the frequency of the wave of interest. The analytical M_2 internal wavelength ranges from about 70 km at the equator to about 300 km at about $10°$ from its critical latitude, where $\omega = f$. The dominant wavelength in our M_2-only two-layer solution, crudely estimated from the maximum of a smoothed spectral estimate of the zonal wavenumber at $10°$ intervals, is plotted over the theoretical curve (Fig. 11). The close agreement suggests that the latitudinal variation in wavenumber is well explained by the linear dispersion relation. Thus our computational grid resolves the semidiurnal baroclinic waves with approximately 10 grid-points at the equator. The K_1 analytical wavelength has also been plotted to illustrate that diurnal frequencies are resolved even better. The ability to resolve all waves increases with latitude. Note the increasing wavelength approaching the critical latitude in both the analytical curves and the modeled internal wave field. Very similar results are found in our 10-layer solution (not shown) indicating that the response is dominated by the first baroclinic mode, even with 10 layers. Space precludes a deeper investigation into the modal response, though it is clearly warranted. Also, while the requisite physics are present in our solution, we have not investigated
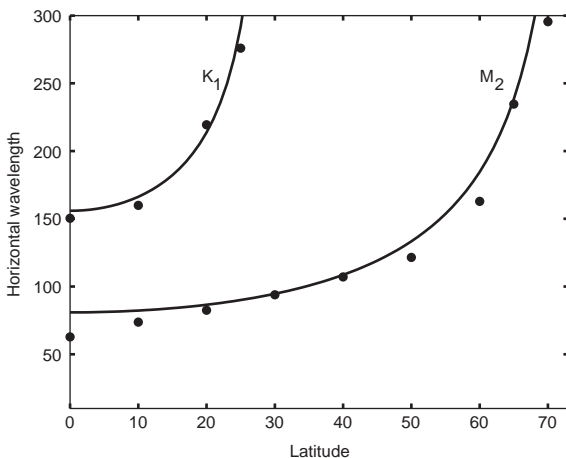
physically important processes that can evolve our internal wave spectrum such as parametric sub-harmonic instability (Olbers, 1983; McKinnon and Winters, 2004).

4.4. Global conversion and tidal rate of work

The renormalized global conversion rate, $\hat{C}$ is 0.67 TW (Table 2) for our two-layer M_2 experiment. Increasing the number of layers to 10 raises this estimate 0.89 TW, an increase of 33%. The work by the M_2 tide on the ocean for our two layer cases is 3.17 TW and is 2.94 TW for our 10-layer case (less work being consistent with a higher conversion rate with 10 layers), with the 10 layer case closer to accepted values. These values are somewhat larger than the 2.54 TW reported by Egbert and Ray (2001), but the agreement is encouraging considering that we are using a tide model that does not assimilate observed tides.

4.5. Regional estimates

Conversion rates from selected regions are labelled in Fig. 12 and tabulated in Table 3. We would like to stress that the place names we have assigned regions are generally for convenience, and are not necessarily meant to imply that a specific geological feature is responsible for the conversion, though in some cases this is certainly the case. For instance "Azores" really indicate a region of rough topography of which the Azores are only a component. In Fig. 13 we present a global map of the renormalized baroclinic energy flux vectors, $\hat{J}$ overlaying a map of barotropic to baroclinic conversion rate. The relationship between internal wave generation, internal wave propagation (see Figs. 6–8), and baroclinic energy flux divergence is clear. Note that the fluxes in the figure have been smoothed with a Hanning window of 2×2 degrees and then sub-sampled in order to give a meaningful large-scale picture of the general pattern and magnitude of fluxes. This smoothing eliminates the many narrow and sinuous beam patterns evident in Fig. 8. Later, we will show a regional map of baroclinic energy flux where the rich details in the flux field are more evident.
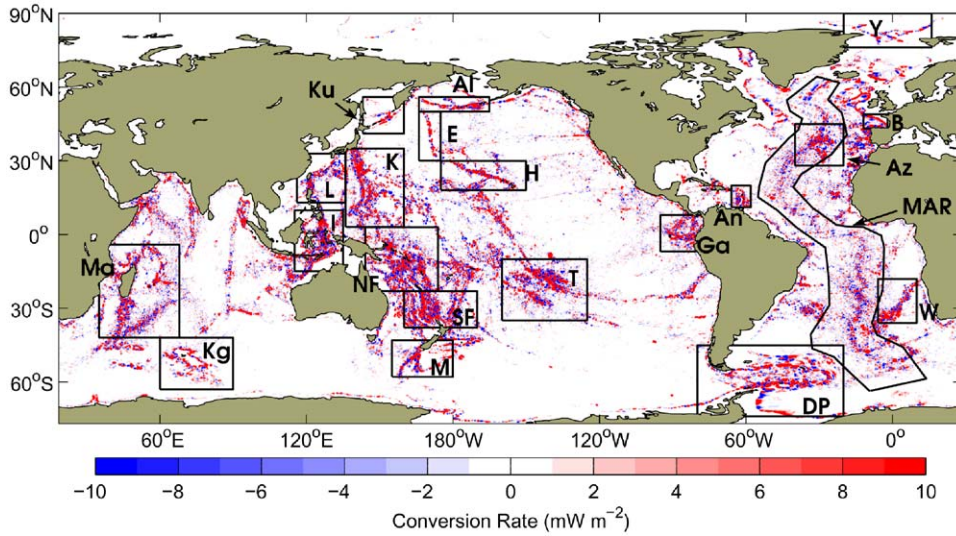

Fig. 11. Theoretical wavelength vs. latitude (solid lines) and wavelength of internal waves (circles) from two layer solution.

Fig. 12. M_2 conversion rate $\hat{C}$ overlayed with regions where area integrated conversion is calculated. Values are tabulated in Table 3. Key: Al = Aleutians Islands/Trench, An = Antilles, Az = Azores, B = Bay of Biscay, DP = Drake Passage/Scotia Sea, E = Emperor Seamounts, SF = South Fiji basin, Ga = Galapagos, H = Hawaii, I = Indonesia, K = Kyushu/Palu Ridge, KG = Kerguelan Plateau, Ku = Kuril Islands/Trench, M = Macquarie Ridge, MA = Madagascar, MAR = Mid-Atlantic Ridge, L = Luzon Strait, NF = North Fiji Basin, T = Tuomoto, W = Walvis Ridge, Y = Fram Strait/Yermak Plateau. Note that the MAR excludes the region delineated by the Azores.

Table 3
Conversion rates, in gigawatts, for various regions of interest (shown in Fig. 12), with comparisons to previous estimates, where available

EXP	Al	An	Az	B	DP	E	Ga	H	I	KG	Ku	K	L	M	MA	NF	SF	T	W	Y	$\sum$	EPR	ABB	MAR	GLOBAL
Two layer (raw)	15	5	19	15	79	3	13	17	54	10	4	25	9	35	25	42	51	40	17	1	478	0.06	0.14	14	648
Ten layer (raw)	19	7	20	14	99	3	14	22	56	15	6	29	16	36	45	55	48	50	19	2	576	0.11	1.46	42	867
Two layer (normalized)	12	7	19	12	34	3	15	23	76	6	3	35	13	28	32	60	55	53	18	1	504	0.07	0.16	12	671
Ten layer (normalized)	15	9	20	11	44	3	17	30	78	9	5	41	22	29	56	79	53	66	20	1	608	0.14	1.62	36	891
Niwa and Hibiya (2001)	10	—	—	—	—	—	—	15	85	—	—	21	41	—	—	39	—	23	—	—	—	—	—	—	—
Merrifield et al. (2001)	—	—	—	—	—	—	—	9	—	—	—	—	—	—	—	—	—	—	—	—	—	—	—	—	—
Kang et al. (2000)	—	—	—	—	—	—	—	5	—	—	—	—	-	—	—	—	—	—	—	—	—	—	—	—	—
Ray and Cartwright (2001)	—	–	–	—	—	—	—	6	—	—	—	—	—	—	—	—	11	—	—	—	—	—	—	—	—
Egbert and Ray (2001)	—	—	—	—	—	—	15	18	—	—	—	47	—	—	—	—	31	—	—	—	—	—	—	103	700 ± 150
Morozov (1995)	—	—	—	—	—	—	—	—	—	—	—	—	—	—	—	—	—	—	—	—	—	—	—	—	1100
Jayne and St. Laurent (2001)	—	—	—	—	—	—	—	—	—	—	—	—	—	—	—	—	—	—	—	—	—	—	—	—	1300
Sjöberg and Stigebrandt (1992)	—	—	—	—	—	—	—	—	—	—	—	—	—	—	—	—	—	—	—	—	—	—	—	—	1070
St. Laurent and Garrett (2002)	—	—	—	—	—	—	—	—	—	—	—	—	—	—	—	—	—	—	—	—	—	0.2	4	—	—
St. Laurent et al. (2003)	—	—	—	—	—	—	—	22	—	—	—	—	—	—	—	—	—	—	—	—	—	—	—	—	—

The first two rows are the raw conversion rates from the model solution. The second two rows are the conversion rates renormalized by Eq. (14). Key: Al = Aleutians Islands/Trench, An = Antilles, Az = Azores, B = Bay of Biscay, DP = Drake Passage/Scotia Sea, E = Emperor Seamounts, Ga = Galapagos, H = Hawaii, I = Indonesia, K = Kyushu/Palu Ridge, KG = Kerguelan Plateau, Ku = Kuril Islands/Trench, M = Macquarie Ridge, MA = Madagascar, MAR = Mid-Atlantic Ridge, L = Luzon Strait, NF = North Fiji Basin, SF = South Fiji basin, T = Tuomoto, W = Walvis Ridge, Y = Fram Strait/Yermak Plateau, EPS = East Pacific Rise, GLOBAL = Global Ocean. The column marked $\sum$ is the sum of the previous columns. The EPR and ABB data are in units of mW m^{-2} and are in locations discussed in St. Laurent and Garrett (2002). Data for Egbert and Ray (2001) is taken from their Table 2, solution TPX0.4a.
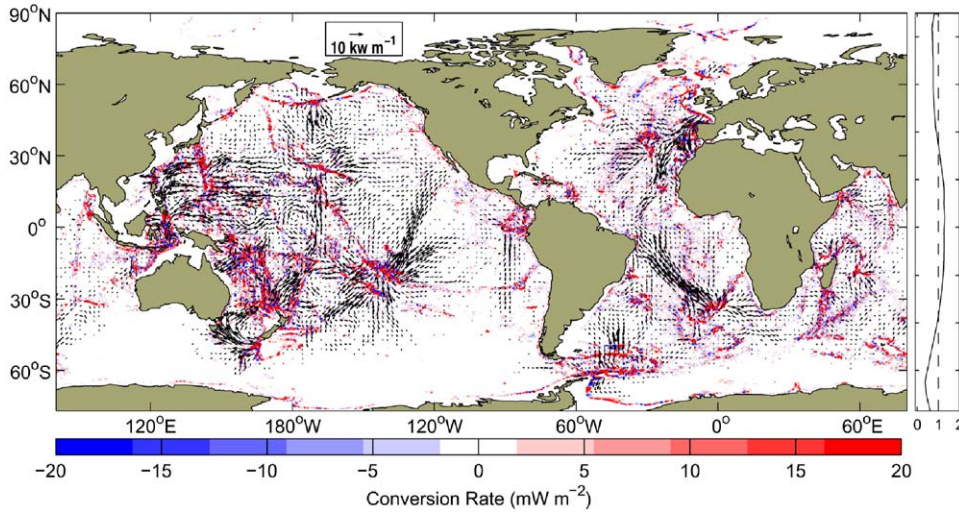
Fig. 13. Baroclinic energy flux $\hat{J}$ and conversion rate $\hat{C}$ from our two-layer simulation, normalized according to (14) and averaged over one tidal cycle. Only a subset of the flux vectors are shown. The zonal mean of the normalization factor (Eq. (14) and Fig. 3) is shown on the right side of the plot. Each vector component has been spatially smoothed with a bidirectional Hanning window with a width set to 2 degrees and then sub-sampled in order to give a meaningful large-scale picture of the general pattern and magnitude of fluxes. For visual clarity it was necessary to make the color range representing the conversion rate be different from Fig. 12, to clip vectors longer than $20\,\mathrm{kW\,m^{-1}}$, and to delete vectors shorter than $1\,\mathrm{kW\,m^{-1}}$.

The conversion is mostly positive (energy transfer is from barotropic to baroclinic motions), and in all of our regional estimates the net conversion is positive. However, over small spatial scales there are regions that are negative. For our two-layer simulations, the total barotropic-to-baroclinic conversion is $+1.40\,\mathrm{TW}$ and the total baroclinic-to-barotropic conversion is $-0.73\,\mathrm{TW}$, adding up to our global conversion of $+0.67\,\mathrm{TW}$. Regions of negative conversion were also found by Egbert and Ray (2001). In our simulation, negative conversion rates arise where there is a convergence of baroclinic energy flux, such as might hypothetically occur between two wavemakers that are an integer number of wavelengths apart and in phase so that the waves constructively interfere. One of the most energetic regions with respect to conversion is the Western Pacific (also noted by Niwa and Hibiya, 2001). The baroclinic energy fluxes emanating primarily northward from Tuomoto in the Pacific and from the Walvis Ridge in the South Atlantic are noteworthy, as is the large flux out of the Bay of Biscay. The marked asymmetry of the fluxes emanating from the Walvis Ridge is particularly interesting.

We note that a number of the regions that are significant generators of baroclinic waves have been commented on previously in the literature, and a global picture with many similarities to ours can be found in Egbert and Ray (2001), hereafter referred to as ER. The level of spatial detail of our conversion calculation allows us to now quantify fluxes for many different geographic features for which there are no previous estimates. The sparseness of the previous estimates in Table 3 reflects this increase in information. There are many regions and features that we could identify as internal wavemakers (our computational grid allows us to make estimates at literally millions of locations). In the interest of brevity, we have limited the number of regions for which we have made explicit estimates. Since we have explicitly simulated internal wave generation by the tides, this lends confidence to the contention of ER that their model misfit is due to the missing physics of baroclinic wave drag in their solution. We also note that the M_2 dissipation presented by ER (their plate 2 and their Table 2) also includes dissipation by quadratic bottom drag. Our map shows *only* the energy flux from the barotropic

mode going in to baroclinic motions (Eq. (11)). We find significant generation of internal waves in many of the regions considered "shallow" by ER (e.g., our Madagascar, Antilles, Luzon Strait, Macquarie Ridge, Kuril Islands, Kerguelan Plateau). For this reason it is difficult for us to compare our two maps in detail. Thus, we will compare with ER only in their "deep" regions where their drag is predominately attributed to baroclinic wave generation. In these regions, we find that our estimate is generally similar to ER's (our Fig. 12 and Table 3). For instance, our 10 layer solution produces a 30 GW conversion rate at Hawaii, as compared to 18 GW found by ER. In general, our estimates are somewhat larger than ER's, and our global, 10 layer M_2 conversion rate is 891 GW, compared to ER's 700 ± 150 GW. Note again that an absolute comparison of our two estimates is not possible because of their combination of work by bottom friction and by implied baroclinic wave drag. Nonetheless, we can speculate that the larger prediction in our solution may be partially attributable to a more energetic tide than ER (and than observed) and partially to ER's exclusion of shallow seas from their estimate. ER do suggest that their estimates may be conservative for this reason.

Our results are also quite similar to the Pacific basin computation of internal tide generation by Niwa and Hibiya (2001), with quantitative comparison of certain regions listed in Table 3. Another notable feature of our solution that is new to our knowledge, is the relatively large internal tide generation by the ridges and trenches surrounding the Scotia Sea. Here, we find as much as $36 \, \text{kW}^{-1} \, \text{m}$ of baroclinic wave energy radiating into the Atlantic, when averaged over an M_2 tidal cycle. The area-integrated conversion rate for the Drake Passage region is as much as 44 GW, or 5% of the global ocean. Naviera-Garabato et al. (2004) have recently inferred strong internal wave activity and mixing in the Scotia Sea, and have speculated as to the geostrophic vs. tidal origin of the observed internal energy in this region. While this study cannot speak for the geostrophic contribution, it does suggest that the internal tide contribution is non-trivial.

Another notable feature of our solutions is the strong conversion at the Walvis Ridge (18–20 GW) in the South Atlantic, with baroclinic energy fluxes radiating north-westward into the South Atlantic, and eastward towards the Indian Ocean. It seems that this site is included in ER's mid-Atlantic Ridge (MAR) estimate. A few of the many additional conversion sites of interest are the Bay of Biscay (15–17 GW), and Cape Farewell (South of Greenland in the Labrador Sea). Note also the generation at the Galapagos and the Lesser Antilles. Ray and Cartwright (2001) estimated that 11 GW are extracted from the barotropic tide at the Tuomoto Archipelago in the South Pacific, about a factor of four smaller than we (53–66 GW), ER (31 GW), or Niwa and Hibiya (23 GW) have found. Note that their estimate of 6 GW for Hawaii is similarly low. Ray and Cartwright suggest that their low estimate for Hawaii is due to poor sampling by the along-track altimeter data used in their study.

A detail of our baroclinic energy flux vectors for our two-layer solution superimposed over Hawaiian topography is shown in Fig. 14. The flux is confined to sinuous, narrow (several hundred kilometer wide) beams emanating irregularly along the ridge. These beams are a ubiquitous feature of our solution (Fig. 8). Chiswell (2002) estimated a baroclinic tidal energy flux of $4.4 \, \text{kW} \, \text{m}^{-1}$ at station Aloha (22.75 N, 158 W), north of Hawaii (indicated in Fig. 14). The flux at this location varies from 0.25 to $7 \, \text{kW}^{-1}$ to the north–west over a tidal cycle with a mean value of $3.5 \, \text{kW} \, \text{m}^{-1}$. The maximum flux along the Hawaiian Ridge is to the north–west, originating from French Frigate Shoals at approximately (24 N, 167 W), ranges over a tidal cycle from 10 to $45 \, \text{kW} \, \text{m}^{-1}$ with a mean value of $26 \, \text{kW} \, \text{m}^{-1}$. Rudnick et al. (2003) reported semidiurnal band fluxes at French Frigate Shoals of $8–34 \, \text{kW} \, \text{m}^{-1}$, which is very similar to what we have obtained here. We find Kauai Channel fluxes of $5–26 \, \text{kW} \, \text{m}^{-1}$ with a mean value of $17 \, \text{kW} \, \text{m}^{-1}$, where Rudnick et al. (2003) measured fluxes of $5–21 \, \text{kW} \, \text{m}^{-1}$. Kang et al. (2000) estimated 5.4 GW along entire Hawaiian ridge ($2.7 \, \text{kW} \, \text{m}^{-1}$) for M_2. Merrifield et al. (2001) found an integrated energy flux away from Hawaii of 9 GW using a baroclinic tide model, but the
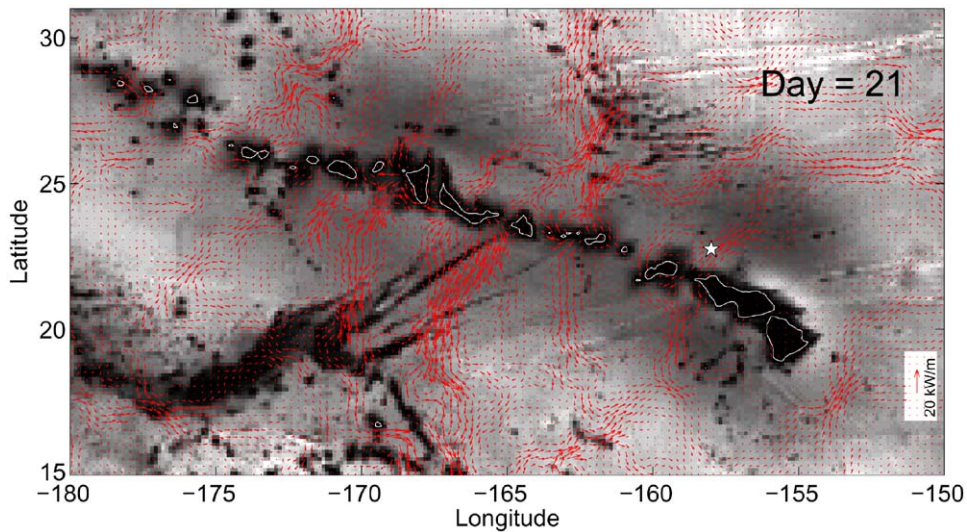
Fig. 14. Detail of baroclinic energy flux vectors near Hawaii for our two-layer solution. The star indicates the location of Station Aloha where Chiswell (2002) estimated a baroclinic tidal energy flux of $4.4\,\mathrm{kW\,m^{-1}}$. Each vector component has been spatially smoothed with a bidirectional Hanning window with a width set to $0.25°$ and then every other vector is plotted. Underlying topography is the model topography at full resolution. A flux of $20\,\mathrm{kW\,m^{-1}}$ is indicated in the lower right-hand corner.

actual conversion was likely larger because they did not account for energy losses within their control volume. Their average baroclinic energy flux was $1.7\,\mathrm{kW\,m^{-1}}$ along the ridge, with a peak value of $10\,\mathrm{kW\,m^{-1}}$. Dushaw (2002) estimated $2.6\,\mathrm{GW}$ for the Hawaiian ridge using altimetry, though he suggests that poor sampling makes this an underestimate. Using a linear theory, St. Laurent et al. (2003) have calculated internal wave generation for a number of abrupt geometries such as a knife-edge, a step, a top-hat ridge, and a top-hat trench. When they apply their theory to the Hawaiian Ridge, they find that as much as $11\,\mathrm{kW\,m^{-1}}$ of internal tide production, or $22\,\mathrm{GW}$ for an $2000\,\mathrm{km}$ ridge.

Another interesting feature of our solutions are the relatively modest contribution from the mid-ocean ridges. St. Laurent and Garrett (2002) used linear theory appropriate to the MAR, and found approximately $4\,\mathrm{mW\,m^{-2}}$ of conversion out of the barotropic M_2 tide at a site on the crest of the MAR. In this latter study, they find that mode-1 internal waves absorb less than 25% of the modal conversion, and that 30 modes are required to account for 80% of the conversion. Note, however, that the net predicted conversion at sites like

this on the MAR is quite small because these high mode internal waves cannot add up to a significant conversion. Our 10-layer solution produces a modest amount of conversion at the same site as St. Laurent and Garrett (2002), with an energy flux of $1.5\,\mathrm{mW\,m^{-2}}$. This is somewhat smaller than the $4\,\mathrm{mW\,m^{-2}}$ predicted by St. Laurent and Garrett (2002) for the total contribution from all modes, but our mode-1 dominated solution agrees well with their estimate that mode-1 carries 25% of the total flux. For their smooth East Pacific rise site we obtain $0.15\,\mathrm{mW\,m^{-2}}$ vs. St. Laurent and Garrett's value of $0.2\,\mathrm{mW\,m^{-2}}$. Our East Pacific rise and Abyssal Brazil Basin estimates are given in Table 3, columns "ABB" and "EPR".

The MAR (excluding the Azores) is responsible for the conversion of $12\,\mathrm{GW}$ in our two-layer simulations, and $36\,\mathrm{GW}$ in our 10-layer solution, the latter accounting for approximately 3% of the global conversion in our 10-layer case. We find that the net conversion integrated over the MAR is comparable to generation sites like Hawaii. It is the huge area of ocean floor occupied by MAR topography that makes the contribution by the MAR at all significant to the global total. In Table 3, column "Σ" we have summed the

contribution for the 20 regions indicated in Fig. 12, but "Σ" does not include the MAR. The total for just these 20 regions is 75% of the global total conversion, yet these regions constitute less than 10% of the ocean sea floor area. Thus, we have found that the globally integrated conversion is dominated by internal wave generation at abrupt topography. In the supercritical theory (i.e., when the slope of internal wave characteristics exceed the slope of the topography) of St. Laurent et al. (2003), the spectrum is red, with 75% of the energy contained in mode-1. In the linear (subcritical) theory of St. Laurent and Garrett (2002) (a modification of Bell, 1975), the mode spectrum is proportional to the product of the bottom stratification, the integrated wavenumber spectrum (the bathymetric variance) and the tidal current. This theory is applicable to topography such as the MAR, predicting that the conversion peaks for mode-5. The conversion associated with this mode is very weak compared to sites where the peaks occurs at or near mode-1, e.g., Hawaii. The topographic roughness along the MAR is dominated by small scales, so that the absolute variance for topographic wavenumber capable of exciting a modal response is small compared to the variance associated with abrupt topographic features such as Hawaii. Thus, as in the linear theory, net conversion is roughly proportional to total topographic variance (Balmforth et al., 2002) and implies that regions like Hawaii are much more efficient at extracting energy from the barotropic tides. For regions like the MAR, mode numbers that are high with respect to our computational grid are required to capture a significant portion of the conversion, and we expect that our estimates will be low. It is interesting to note that our 10-layer solution, which can admit some higher modal response, does result in an 80% increase of conversion integrated over the MAR; in regions of abrupt topography, where generation is biased towards low modes, our solutions are generally very similar for both two and 10 layers. Presumably regions like the MAR will become more important as resolution increases, both vertically and horizontally, allowing a more realistic mode spectrum to be excited.

5. Summary and conclusions

A process-oriented study of the rate of conversion of the barotropic tide into baroclinic waves and the rate of working of the ocean by tidal forces has been conducted using a isopycnic coordinate ocean model. The accuracy of our tidal elevations is comparable to the accuracies found in un-tuned tidal simulations that do not assimilate data (Jayne and St. Laurent, 2001; Arbic et al., 2004; Egbert et al., 2004). With an overly energetic barotropic tide our tidal solutions produce a rich global field of internal waves. The baroclinic energy flux associated with propagating internal waves is concentrated in beams that extend thousands of kilometers from generations sites. We find a total of 2.94 TW of work is done by the M_2 tides in our 10-layer experiment, close to previous estimates. The globally integrated conversion with two layers is 0.67 TW. Our 10 layer estimate is 0.89 TW, which is close to the 0.7 ± 0.15 TW estimate of Egbert and Ray (2001), but note that they did not include many shallow regions (e.g., Fig. 13 and Table 3 denoted Madagascar, Lesser Antilles, Luzon Strait, Macquarie Ridge, Kuril Islands, Kerguelan Plateau) where we find significant internal wave generation.

Our solution captures many of the internal wave generation sites previously noted in the literature, and the model suggests many generation sites that to our knowledge have not been previously noted. Several such sites are the Scotia Ridge and Sandwich Islands and the Walvis Ridge in the South Atlantic. We are also able to make quantitative estimates of regional conversion that not have been made previously. Approximately 75% of the global conversion of barotropic tides into internal waves is accounted for by 20 internal wave generation sites (Table 3). In these hot-spots, the conversion rates and baroclinic energy fluxes compare well with previously available regional estimates. These are regions of abrupt topography, and dominate generation from sites such as the MAR. Thus conversion is dominated by low mode internal wave generation at regions of large net topographic variance such as trenches and island arcs. The fact that estimates compare favorably in regions where other estimates have been made give

us confidence that our solution has value as a prognostic tool for estimating fluxes in new regions. The quantitative estimate of the conversion is limited by the dependence on the local value of stratification. To account for spatially varying stratification, we have employed an a posteriori WKB-like renormalization (Eqs. (14) and (15)). Note that the magnitude of this renormalization is relatively modest and does not change the qualitative features of mode conversion, baroclinic wave generation and baroclinic energy flux.

The baroclinic response is primarily in the first internal mode even for our 10-layer solution. Evidence for this is the close agreement (for both the two and 10-layer solutions) between the internal wavelengths and those predicted by the two layer dispersion relationship. While we have not yet undertaken a full modal analysis of our 10-layer solution, there is some evidence that higher modes are being excited. Indications are the 33% higher conversion rates for our 10-layer solution (Table 3), the disturbance of isopycnals near roughness elements near the ocean bottom (Fig. 9), and the marked increase of conversion in the Abyssal Brazil Basin and East Pacific Rise. We regard the low-mode internal wave generation, and associated conversion from to barotropic to baroclinic motions to be represented in a physically robust manner. Our resolution, both horizontal and vertical, is suitable, by construction, to resolving the low modes. The increase of conversion at the Abyssal Brazil Basin and East Pacific Rise with increased vertical resolution are suggestions that as we increase horizontal and vertical resolution, these sites will become more important contributors. However, since we already obtaining nearly one TW of conversion with two layers, it is unlikely that the unresolved higher modes will account for a great deal more net conversion.

We have found that the adiabatic generation of low-mode internal tides is insensitive to many of the parameterizations that finite-difference models must employ (see our appendix), but are reluctant at this stage to make conclusions about the fraction of internal wave energy lost to local dissipation to that radiated far away from the generation site. We acknowledge that there are many aspects of the solution to which an ocean general circulation model are not well suited. The accurate determination of how much of energy extracted from the barotropic tides is dissipated locally versus the amount radiated away cannot be captured accurately by our adiabatic model, because it cannot support the higher mode internal wave generation and turbulence that mediate this partitioning. With respect to this latter point, however, some theory suggests that low-mode waves are stable over times long relative to their fundamental frequency, and therefore our qualitative picture of adiabatic internal wave generation and energy redistribution by baroclinic energy fluxes radiating away from generation regions is likely a reasonable first-order description, even if the ultimate decay of these waves cannot be resolved explicitly for the foreseeable future.

Acknowledgements

Appendix A

A.1. Details of model configurations

The basic experiments ("two-layer", "ten-layer") discussed in the main part of this paper had the following configuration. Horizontal resolution was one-eighth degree. Biharmonic isopycnal viscosity was set by a parameter, A, which is

multiplied by third power of the grid resolution. This parameter has units of velocity and was set to $0.01\,\mathrm{m\,s^{-1}}$. The scalar self-attraction and loading parameter (SAL) was 0.094. The time step for the baroclinic mode was 80 s, and 10 s for the barotropic mode, i.e., a split timestep of eight-to-one. The non-dimensional quadratic bottom drag coefficient was 0.003. Vertical viscosity was set to the molecular value of $10^{-6}\,\mathrm{m^2\,s^{-1}}$. Diapycnal mixing was zero in order to focus on the *adiabatic* generation of baroclinic internal waves.

We also conducted a number of additional simulations to assess the sensitivity of conversion rate to the following: horizontal resolutions of half, quarter, eighth, and sixteenth degree; specified constant diapycnal mixing ranging from 0 to $10^{-4}\,\mathrm{m^2\,s^{-1}}$; biharmonic viscosity variations of two orders of magnitude, from 0.01 to $1.0\,\mathrm{m\,s^{-1}}$; vertical viscosity ranging from $10^{-6}\,\mathrm{m^2\,s^{-1}}$ (molecular) to $10^{-4}\,\mathrm{m^2\,s^{-1}}$; filtering to reduce topographic roughness; bottom drag coefficient ranging from 0.003 to 0.3; SAL parameter of 0.084 or 0.094; either one (M_2 only) or the eight dominant tidal constituents. The barotropic time step for the four resolutions explored was 50, 25, 10, and 5 s for the half, quarter, eighth, and sixteenth degree numerical experiments, respectively. To assess the impact of split time stepping, the ratio of baroclinic to barotropic mode time-steps was additionally varied from sixteen-to-one to one-to-one.

Topography data was taken from the thirtieth-degree resolution ETOPO2 dataset (National Geophysical Data Center), down-sampled to the target grids ($\frac{1}{2}, \frac{1}{4}, \frac{1}{8}, \frac{1}{16}$ degree) by a simple nearest neighbor scheme without any pre-filtering, except when sensitivity to topographic roughness was investigated.

A.2. Sensitivity of results

Of the factors listed above, the only factors responsible for producing more than a 10% difference in global conversion rate are increasing horizontal and/or vertical resolution, filtering topography to reduce roughness, increasing the number of tidal constituents included in the forcing, and increasing the bottom drag coefficient. A

bottom drag coefficient of 0.03, a factor of 10 time larger than is physically justifiable, had approximately a 10% effect on the globally integrated convergence. A coefficient of 0.3 reduced the conversion rate by a factor of two, and as such is significant. However, we feel that this is an unphysical parameter choice. Note, however, that it does result in more realistic barotropic tidal energy levels. This subject is addressed carefully by Arbic et al. (2004). Adjusting horizontal and vertical viscosity, diapycnal mixing and SAL all resulted in negligible changes to the solution. Based on these findings about parameter sensitivity, we will report only the effects of topographic roughness, vertical and horizontal resolution, and the number of tidal constituents.

A.2.1. Two layers

Global conversion more than doubles going from half to quarter degree resolution, but increases by less than 10% going to eighth degree. Going to one-sixteenth degree resolution only adds another 1%, so that our highest explicitly resolved conversion is 0.68 TW. The implication is that the topography that excites the mode-1 response has been adequately resolved at one-eighth degree. Higher horizontal resolution is required to resolve topographic wavenumbers capable of exciting a higher mode response, but, by construction, only mode-1 can be excited in a two layer system. Therefore, the 1% increase in convergence going from eighth to sixteenth degree resolution leads us to believe that the solution has converged in the physical (albeit not the mathematical) sense. Because of this apparent convergence, also we conclude that higher modes potentially excited by increasingly resolved high wavenumber topography are not spuriously projected into the gravest internal mode. We have extrapolated the two-layer case to zero grid spacing (the continuous limit). This gives us the estimate that the system removes 0.69 TW of energy from the barotropic M_2 tide.

A.2.2. Ten layers

The conversion increased by 30% going from quarter to eighth degree resolution, whereas our two-layer solution had less than a 10% increase

over this horizontal resolution transition. There is an additional 7% increase going to one-sixteenth degree. Our highest resolution (one-sixteenth degree horizontally, 10 layers vertically) explicitly resolved conversion is 1.00 TW. In the continuous limit, this conversion is extrapolated to 1.04 TW. The fact that the conversion rate increases with horizontal resolution when there are more than two layers is an indication that additional degrees of freedom are admitted with more layers. This higher mode number response can be seen in the section view of Fig. 9. The moderately increasing conversion (as compared to two-layer solutions) with respect to increasing horizontal resolution for these experiments suggests that these higher mode number fluxes are not entirely resolved.

A.2.3. Sensitivity to topographic roughness

Fig. 15 compares the wavenumber spectrum of filtered and unfiltered topography, used to investigate the sensitivity to bottom roughness. The filtering was a five-point bi-directional Hanning window applied both meridionally and zonally. For our basic experiments, direct interpolation of our source topography to our model grid by a nearest neighbor scheme most nearly preserves the roughness present in the source data, as measured

by the topographic wavenumber spectrum (Fig. 15). Smoothing the source topography prior to regridding, as is common in terrain-following and geopotential coordinated models results in a loss of topographic variance at high wavenumbers and reduces the conversion rate by approximately 50% at one-quarter degree for both the two and 10-layer cases. However, at one-eighth degree the conversion rate is only reduced by 24%. This is evidence that the length scales responsible for generating mode-1 internal waves are better resolved by eighth degree resolution, so that filtering has less of an effect. At a quarter degree, the conversion rate reduction after filtering is the same for two and 10 layer solutions. This further suggests that the filtering at lower resolution has eliminated spatial scales responsible for generating higher mode response.

A.2.4. Sensitivity of the work done by the tides

The work done by the tidal forcing, T, reduces with increased horizontal resolution, and is estimated to be 2.5 TW in the horizontally continuous 10-layer limit for the M_2 tide. The addition of eight constituents raises the global work by approximately 40%. Again assuming that the eight-constituent system converges like the M_2-only system, we estimate T for the eight primary tidal constituents to be 3.7 TW. Ten layers makes less than a 4% difference to the estimate. Inclusion of eight constituents raises T to 3.94 TW, which is approximately 10% larger than the accepted value of 3.5 TW.

A.2.5. Multiple constituent runs

With eight constituents, we find that the tides do not energetically equilibrate in the same manner as the single constituent case, and there is considerable variability in the globally integrated energy budget (Fig. 16) with clear spring-neap and longer period variations occurring. These longer period variations arise because of frequency beating of the forcing. The model is integrated for 60 days, with our analysis based on an average over the last three fortnightly cycles. It is interesting that the work done by frictional dissipation lags the work done by tides by several days. This time lag is likely to be sensitive to our parameterization of
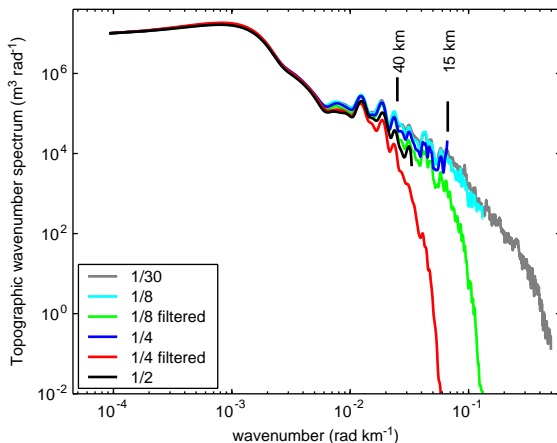

Fig. 15. Effect of spatial pre-filtering on wavenumber spectra of topography for a zonal section through Drake Passage. Note that the *spectrum* has been smoothed to improve clarity. The topography is downsampled through a simple nearest neighbor scheme.
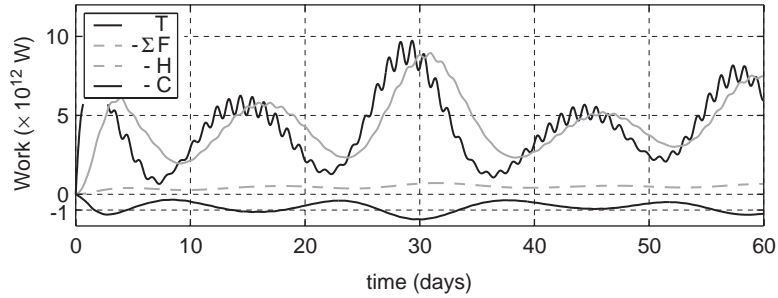
Fig. 16. Time-series of various terms in global energy budget for an eight constituent experiment. The data has been low-pass filtered to remove the semidiurnal variability. The labels in the legend are T, the total work by the tidal forcing, ΣF, the total work done by friction, H, the work done by horizontal friction, and C, the barotropic to baroclinic conversion rate.
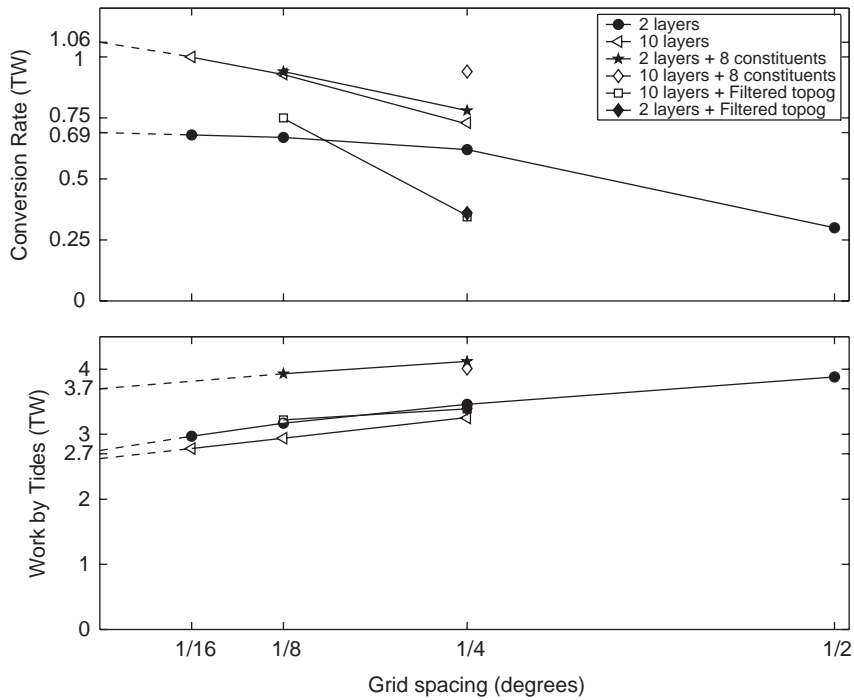

Fig. 17. Top panel: Conversion rate vs. horizontal resolution. Bottom panel: work by tide vs. horizontal resolution.

friction. The globally integrated conversion (discussed in Section 4.4) is also shown because it is interesting to note its long period modulation. The two-layer conversion is 0.94 TW, a 40% increase over our M_2-only solution. We can thus estimate that a 10-layer ocean would have a conversion of 1.3 TW. Assuming that the eight-constituent con-

version has similar convergence properties with respect to horizontal resolution to that of M_2-only solutions, we estimate that in the two-layer horizontally continuous limit, the net conversion is 0.96 TW. Our estimate for the conversion in a 10 layer system is 1.34 TW, which is similar to, but slightly larger than the Egbert and Ray (2001)

value of $1 \pm 0.25\,\mathrm{TW}$ estimate. Using the ratio of two-layer M_2-only to two-layer eight constituent tidal rate of work, we can estimate that the eight constituent 10 layer tidal rate of work to be $3.64\,\mathrm{TW}$. Finally, a notable feature of the eight constituent experiments is a markedly increased conversion in the Western Pacific, particularly at Luzon Strait, where our conversion jumps from less than $22\,\mathrm{GW}$ for our 10-layer M_2 solution, to $46\,\mathrm{GW}$ for eight constituents.

A.2.6. Summary of sensitivity experiments

One of our goals of this study has been to establish some basic data about the resolution and computational expense necessary to meaningfully capture internal tide generation in a numerical model at the global scale. We have demonstrated the feasibility of global baroclinic simulations by showing that the conversion rates of barotropic to low-mode baroclinic tidal energy converge as a function of resolution. The first baroclinic mode appears to be adequately resolved at one-eight degree, and even one-quarter degree grids can produce meaningful results. Higher modes admitted by our 10-layer solution appear to be only partially resolved at one-sixteenth degree. Substantiated by the convergence in the conversion rate, the insensitivity to parameterization of viscous stresses and diapycnal mixing, and favorable comparison to independent estimates of conversion and baroclinic energy flux, it is suggested that numerical models can be a useful tool in understanding the internal tide generation problem (Fig. 17).

References

Alford, M.H., 2003. Redistribution of energy available for ocean mixing by long-range propagation of internal waves. Nature 423, 159–162.

Althaus, A., Kunze, E., Sanford, T., 2003. Internal tide radiation from Mendecino Escarpment. Journal of Physical Oceanography 33, 1510–1527.

Antonov, J.I., Levitus, S., Boyer, T.P., Conkright, M.E., O'Brien, T.D., Stephens, C., 1998. World Ocean Database 1998. vol. 4: Salinity of the Atlantic Ocean. Technical Report, NOAA Atlas NESDIS 30, US Government Printing Office, Washington, DC, 166 pp.

Arbic, B., Garner, S., Hallberg, R., Simmons, H., 2004. The accuracy of surface elevation in forward global barotropic and baroclinic tide models. Deep-Sea Research II, this issue [doi:10.1016/j.dsr2.2004.09.014].

Baines, P., 1973. The generation of internal tides by flat-bump topography. Deep-Sea Research 20, 179–205.

Baines, P.G., 1982. On internal tide generation models. Deep-Sea Research 29, 307–338.

Balmforth, N., Ierley, G., Young, W., 2002. Tidal conversion by subcritical topography. Journal of Physical Oceanography 32, 2900–2914.

Bell, T.H., 1975. Lee waves in stratified flows with simple harmonic time dependence. Journal of Fluid Mechanics 67, 705–722.

Bleck, R., Smith, L., 1990. A wind-driven isopycnic coordinate model of the North and Equatorial Atlantic Ocean. 1. model development and supporting experiments. Journal of Geophysical Research 95, 3273–3285.

Boyer, T.P., Levitus, S., Antonov, J.I., Conkright, M.E., O'Brien, T.D., Stephens, C., 1998. World Ocean Database 1998. vol. 1: Temperature of the Atlantic Ocean Technical Report, NOAA Atlas NESDIS 27, US Government Printing Office, Washington, DC, 166 pp.

Chiswell, S.M., 2002. Energy levels, phase, and amplitude modulation of the baroclinic tide off Hawaii. Journal of Physical Oceanography 32, 2640–2651.

Cummins, P., Oey, L., 1997. Simulation of barotropic and baroclinic tides off Northern British Columbia. Journal of Physical Oceanography 27, 762–781.

Cummins, P.F., Cherniawski, Y., Foreman, M., 2001. North Pacific internal tides from the Aleutian Ridge, altimeter observations and modeling. Journal of Marine Research 59, 167–191.

Dushaw, B., 2002. Mapping low-mode internal tides near hawaii using TOPEX/POSEIDON altimeter data. Geophysical Research Letters 29, 10.1029/2001GL013944.

Dushaw, B., Worcester, P., Cornuelle, B., Howe, B., 1995. Barotropic and baroclinic tides in the central North Pacific Ocean determined from long-range reciprocal acoustic transmissions. Journal of Physical Oceanography 25, 631–647.

Egbert, G.D., Erofeeva, S.Y., 2002. Efficient inverse modeling of barotropic ocean tides. Journal of Atmospheric and Oceanic Technology 19, 183–204.

Egbert, G., Ray, R., 2000. Significant dissipation of tidal energy in the deep ocean inferred from satellite altimeter data. Nature 405, 775–778.

Egbert, G.D., Ray, R.D., 2001. Estimates of M_2 tidal energy dissipation from TOPEX/POSEIDON altimeter data. Journal of Geophysical Research 106, 22475–22502.

Egbert, G.D., Ray, R.D., Bills, B.G., 2004. Numerical modelling of the global semidiurnal tide in the present day and in the Last Glacial Maximum. Journal of Geophysical Research 109, doi:10.1029/2003JC001973.

Gill, A.E., 1982. Atmosphere-Ocean Dynamics. International Geophysics Series, vol. 30. Academic Press, New York, 662 pp.

Hallberg, R., 1997. Stable split time stepping schemes for large-scale ocean modeling. Journal of Computational Physics 135, 54–65.

Hallberg, R., Rhines, P., 1996. Buoyancy-driven circulation in an ocean basin with isopycnals intersecting the sloping boundary. Journal of Physical Oceanography 26, 914–940.

Hendershott, M.C., 1972. The effects of solid earth deformation on global ocean tides. Geophysical Journal of the Royal Astronomical Society 29, 389–402.

Hendry, R.M., 1977. Observations of the semidiurnal internal tide in the western North Atlantic Ocean. Philosophical Transactions of the Royal Society of London A 286, 1–24.

Hibiya, T., 1986. Generation mechanism of internal waves by tidal flow over a sill. Journal of Geophysical Research 91, 7696–7708.

Holloway, P.E., Merrifield, M., 1999. Internal tide generation by seamounts, ridges, and islands. Journal of Geophysical Research 104, 25937–25951.

Jayne, S.R., St Laurent, L.C., 2001. Parameterizing tidal disspiation over rough topography. Geophysical Research Letters 28, 811–814.

Kang, S., Foreman, M., Crawford, W., Cherniawsky, J., 2000. Numerical modeling of internal tide generation along the Hawaiian ridge. Journal of Physical Oceanography 30, 1083–1098.

Kantha, L., Tierney, C., 1997. Global baroclinic tides. Progress in Oceanography 40, 163–178.

Kowalik, Z., Polyakov, I., 1999. Diurnal tides over Kashevarov Bank, Okhotsk Sea. Journal of Geophysical Research 104, 5361–5380.

Kunze, E., Toole, J.M., 1997. Tidally driven vorticity, diurnal shear, and turbulence atop Fieberling Seamount. Journal of Physical Oceanography 27, 2663–2693.

Kunze, E., Rosenfeld, L.K., Carter, G.S., Gregg, M.C., 2002. Internal waves in Monterey submarine canyon. Journal of Physical Oceanography 32, 890–913.

Leaman, K., Sanford, T., 1975. Vertical energy propagation of inertial waves: a vector spectral analysis of velocity profiles. Journal of Geophysical Research 80, 1975–1978.

Ledwell, J.R., Watson, A.J., Law, C.S., 1993. Evidence for slow mixing across the pycnocline from an open-ocean tracer-release experiment. Nature 364, 701–703.

Ledwell, J.R., Watson, A.J., Law, C.S., 1998. Mixing of a tracer released in the pycnocline of a subtropical gyre. Journal of Geophysical Research 103, 21499–21529.

Ledwell, J.R., Montgomery, E.T., Polzin, K.L., Laurent, L.C.S., Schmitt, R.W., Toole, J.M., 2000. Mixing over rough topography in the Brazil Basin. Nature 403, 179–182.

Lien, R.-C., Gregg, M.C., 2001. Observations of turbulence in a tidal beam and across a coastal ridge. Journal of Geophysical Research 106, 4575–4591.

Lueck, R., Mudge, T., 1997. Topographically induced mixing around a shallow seamount. Science 276, 1831–1833.

Marchuk, G.I., Kagan, B.A., 1984. Ocean Tides: Mathematical Models and Numerical Experiments. Pergamon Press, Oxford.

McKinnon, J., Winters, K., 2004. Reconsidering a disqualified candidate for the energy balance of oceanic internal waves. EOS Transactions of the American Geophysical Union 84 (52), OS12G-07.

Merrifield, M.A., Holloway, P., Johnston, T., 2001. The generation of internal tides at the Hawaiian ridge. Geophysical Research Letters 28, 559–562.

Morozov, E., 1995. Semidiurnal internal wave global field. Deep-Sea Research I 42, 135–148.

Moum, J.N., Caldwell, D.R., Nash, J.D., Gunderson, G.D., 2002. Observations of boundary mixing over the continental slope. Journal of Physical Oceanography 32, 2113–2130.

Munk, W., 1981. Internal waves and small-scale processes. In: Warren, B.A., Wunsch, C. (Eds.), Evolution of Physical Oceanography—Scientific Surveys in Honor of Henry Stommel. MIT Press, Cambridge, MA, pp. 264–291.

Munk, W., 1997. Once again: once again-tidal friction. Progress in Oceanography 40, 7–35.

Munk, W.H., Wunsch, C., 1998. Abyssal recipes II: energetics of tidal and wind mixing. Deep-Sea Research I 45, 1977–2010.

Murray, R.J., 1996. Explicit generation of orthogonal grids for ocean models. Journal of Computational Physics 126, 251–273.

Naviera-Garabato, A.C., Polzin, K., King, B., Heywood, K.J., Visbeck, M., 2004. Widespread intense turbulent mixing in the Southern Ocean. Science 303, 210–213.

Niwa, Y., Hibiya, T., 2001. Numerical study of the spatial distribution of the M_2 internal tide in the Pacific Ocean. Journal of Geophysical Research 106, 22229–22441.

Olbers, D.J., 1983. Models of the oceanic internal wave field. Reviews of Geophysics 21, 1567–1606.

Pinkel, R., Munk, W., Worcester, P., et al., 2001. Ocean mixing studied near the Hawaiian Ridge. EOS Transactions of the American Geophysical Union 81, 545,553.

Polzin, K.L., Toole, J.M., Ledwell, J.R., Schmitt, R.W., 1997. Spatial variability of turbulent mixing in the abyssal ocean. Science 276, 93–96.

Ray, R., Cartwright, D.E., 2001. Estimates of internal tide energy fluxes from Topex/Poseidon altimetry: Central North Pacific. Geophysical Research Letters 28, 1259–1262.

Ray, R., Mitchum, G., 1996. Surface manifestation of internal tides generated near Hawaii. Geophysical Research Letters 23, 2101–2104.

Ray, R., Mitchum, G., 1997. Surface manifestation of internal tides in the deep ocean: observations from altimetry and tide gauges. Progress in Oceanography 40, 135–162.

Ray, R.D., 1998. Ocean self-attraction and loading in numerical tidal models. Marine Geodesy 21, 181–192.

Rudnick, D., Boyd, T.J., Brainard, R.E., Carter, G.S., Egbert, G.D., Gregg, M.C., Holloway, P.E., Klymak, J.M., Kunze, E., Lee, C.M., Levine, M.D., Luther, D.S., Martin, J.P., Merrifield, M.A., Moum, J.N., Nash, J.D., Pinkel, R., Rainville, L., Sanford, T.B., 2003. From tides to mixing along the Hawaiian ridge. Science 301, 355–357.

Sadourny, R., 1975. The dynamics of finite-difference models of the shallow water equations. Journal of Atmospheric Science 32, 680–689.

Sjöberg, B., Stigebrandt, A., 1992. Computations of the geographical distribution of the energy flux to mixing processes via internal tides and the associated vertical circulation in the ocean. Deep-Sea Research 39, 269–291.

St. Laurent, L.C., Garrett, C., 2002. The role of internal tides in mixing the deep ocean. Journal of Physical Oceanography 32, 2882–2899.

St. Laurent, L.C., Stringer, S., Garrett, C., Perrault-Joncas, D., 2003. The generation of internal tides at abrupt topography. Deep-Sea Research I 50, 987–1003.

Wahr, J., 1981. Body tides on an elliptical rotating elastic and oceanless earth. Journal of the Royal Astronomical Society 64, 677–703.

Webb, D.J., Suginohara, N., 2001. The interior circulation of the ocean. in: Siedler, G., Church, J., Gould, J. (Eds.), Ocean Circulation and Climate, International Geophysics Series, vol. 77. Academic Press, New York, 715pp.

Xing, J., Davies, A.M., 1998. A three-dimensional model of internal tides on the Malin-Hebrides shelf and shelf edge. Journal of Geophysical Research 103, 27821–27847.